

Topological Shape Optimization Design of the Whole Bead of 265/35R18 Steel-Belted Radial Tire

Yong Li¹, Shuang Zhang¹, Tao Wang¹, Kai Zhang¹, Long Chen^{2,*} and Shanling Han^{1,*}

¹College of Mechanical and Electronic Engineering, Shandong University of Science and Technology, Qingdao, 266590, China

²College of Materials Science and Engineering, Shandong University of Science and Technology, Qingdao, 266590, China

Abstract: The tire bead, as the most important load-bearing component at the bead area, is closely related to the durability of the tire, but its structure is developing slowly. For this reason, the topological whole bead design was proposed, although it performs well, many defects existed due to the design based on traditional experience. Therefore, this paper studies the topology shape optimization algorithm, delves into the main criterion based on von Mises and the interlaminar shear stress, and provides guidance for the structurally optimal design of the 265/35R18 radial tire whole bead. The finite element simulation results show that the von Mises of the inner end of the chafer and the end of the carcass cord are reduced by 14.48% and 24.12%, respectively. The interlaminar shear stress decreased by 28.96% and 49.51%, respectively. The von Mises of chafer and carcass cord decreased by 13.17% to 40.36% and 7.71% to 20.51%, respectively. The optimization design is of great significance to further improve the safety performance of tires.

Keywords: Radial tire, topological whole bead, finite element simulation, topology shape optimization, interlaminar shear stress criterion.

1. INTRODUCTION

Because the structure of a tire is primarily made up of flexible composite materials combined with rubber and steel cord [1], under the combined action of periodic load, ground friction, and mutual friction of materials inside the structure, it will cause deformation and hysteresis damage of the rubber and skeleton, followed by temperature rise, resulting in slow damage of the rubber materials within the tire and fatigue damage of the internal skeleton. Experts, academicians, and companies are therefore focusing their tire research efforts on how to improve and enhance tire durability and damage resistance, thereby reducing tire faults, extending tire life, and enhancing safety.

Figure 1 depicts the symptoms of a damaged tire, which are primarily localized in the crown, shoulder, sidewall, and bead regions. During the manufacturing process, oxygen from the steel cord inside the structure will travel to the ends of the cord, resulting in thermal oxygen aging. The elevated shear stress at the end of the steel cord causes a significant increase in temperature, and the intersection of various rubber

interfaces causes a step in the stress field. Consequently, tire fatigue damage is most prevalent in cord-and-rubber composites. As depicted in Figure 2, nearly half of all annual tire quality issues are attributable to bonding defects such as lack of adhesive and delamination in the tire bead area [2], the most complex area of the tire structure. Once a macroscopic fracture forms in this region, it rapidly enlarges under the influence of thermal oxygen aging and shear, resulting in instantaneous air leaks and even tire rupture. Therefore, the safety performance of the bead area part is crucial to the vehicle's protection [3].

In practice, the tire bead is the primary load-bearing component of the bead area, and it also makes contact with a number of other components. The bead structure has a significant impact on the distribution of stresses in the bead region. Therefore, it is of utmost significance to improve the safe working life of tires by studying the problem of tire bead area damage and optimizing the bead structure of the tire bead area.

As a region with a high incidence of tire disease, the bead area's quality has a significant impact on the efficacy of the tire. Linden *et al.* [4] noted that changing the material and optimizing the structure of the tire can enhance the pressure distribution of the contact between the tire and the rim. This study offers recommendations for optimizing tire structure. Zhang *et al.* [5] focused primarily on the crack expansion trend

*Address correspondence to these authors at the College of Mechanical and Electronic Engineering, Shandong University of Science and Technology, Qingdao, 266590, China; E-mail: hanshanling@sdust.edu.cn

College of Materials Science and Engineering, Shandong University of Science and Technology, Qingdao, 266590, China; E-mail: chenlongc414@126.com



Figure 1: The diseases of tire bead area, sidewall and shoulder parts.

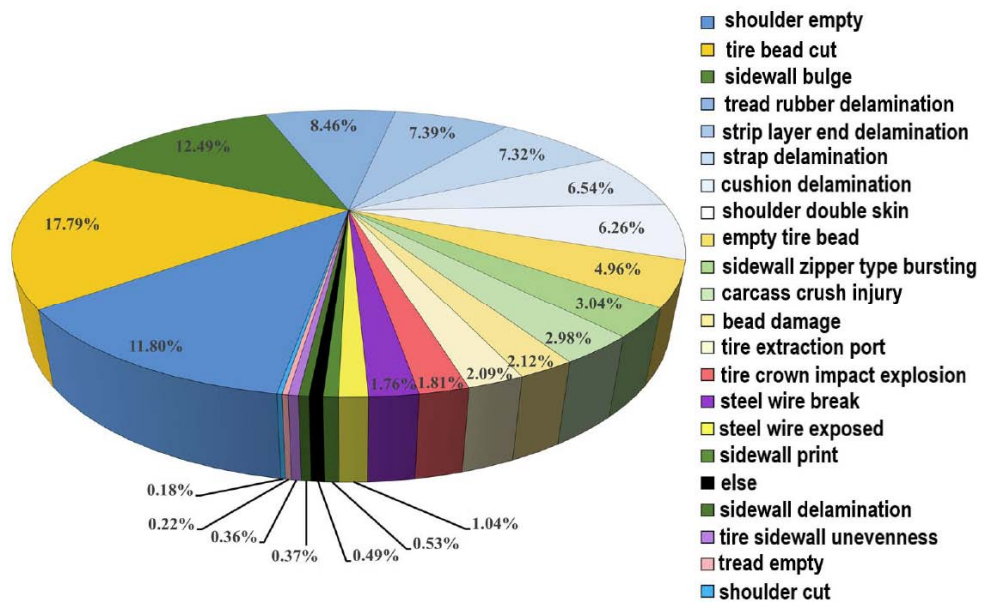


Figure 2: Distribution ratio of various diseases of radial tire [2].

and growth angle of radial tire bead under inflation conditions and contemplated using more durable bead materials or altering bead structure to mitigate the risk of crack expansion. Pawel *et al.* [6] investigated the relationship between the tire fiber structure and the energy absorbed by the tire through a comparative analysis of the basic tire model and the optimized tire model's tire components. This study demonstrates that optimizing the cord angle configuration can reduce local tire damage and enhance its anti-explosion

performance. Yu *et al.* [7] examined the tire deterioration mechanism. By redesigning the structure of the airtight layer and the cord layer, it is possible to effectively enhance the stress concentration in the bead area as well as the durability and damage resistance of tires. The triangle elastomer is in direct contact with the bead, and the modification of its structure also affects the bead's performance. Peter *et al.* [8] investigated the relationship between the structural form of the bead component and the

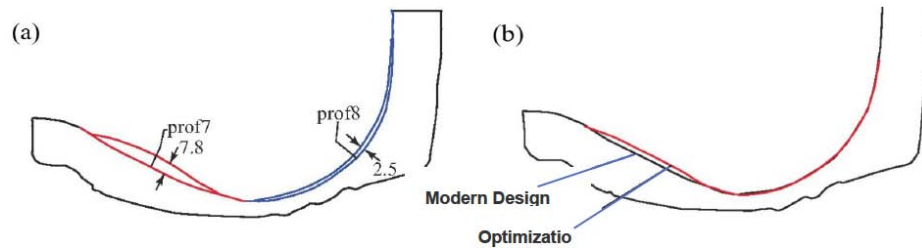


Figure 3: The optimization design of the tire bead area: (a) the contour modification in the bead area; (b) comparison of the contours in the bead area before and after optimization [9].

performance of the tire and rim assembly. By optimizing the geometry of the apex rubber in contact with the bead, the problem of residual air on the contact surface is reduced during assembly of the apex rubber and bead in the bead area.

The aforementioned academics have devised ideas for optimizing the bead structure in order to enhance the tire's performance. Although they have not yet proposed a practicable optimization scheme, they have indicated how the bead structure can be optimized. Sanjeev *et al.* [10] used a numerical method to optimize the bead design of a gas-free tire. Instead of engineering elastic materials, ordinary elastic materials and polyester materials are used. Comparative studies indicate that tires with circular structures and engineering materials have less torsion. This study proposes bead structure optimization strategies that can effectively enhance tire performance and service life.

The bead is a complex tension concentration area that has a significant impact on the tire's safety and durability. As shown in Figure 4, numerous institutions have conducted extensive research and investigations based on the traditional tire bead. Pirelli has investigated several designs for enhanced tire rings: Multiple annular tensile reinforcing elements comprise a shape memory alloy bead capable of producing an elastic clamping force at a predetermined temperature and progressively increasing the contraction force with increasing temperature. A composite tire bead constructed from steel wire and carbon fiber to increase clamping force and torsional rigidity while decreasing tire weight. (e) improve the bead structure and permit the neutral profile of the cord layer to travel through the ring, thereby reducing the torque of the carcass cord acting on the ring and decreasing the risk of ring fatigue failure. Michelin devised (b) the tire bead with geometric roll structure characteristics, wherein the tire cord layer is wound on the outside of the tire

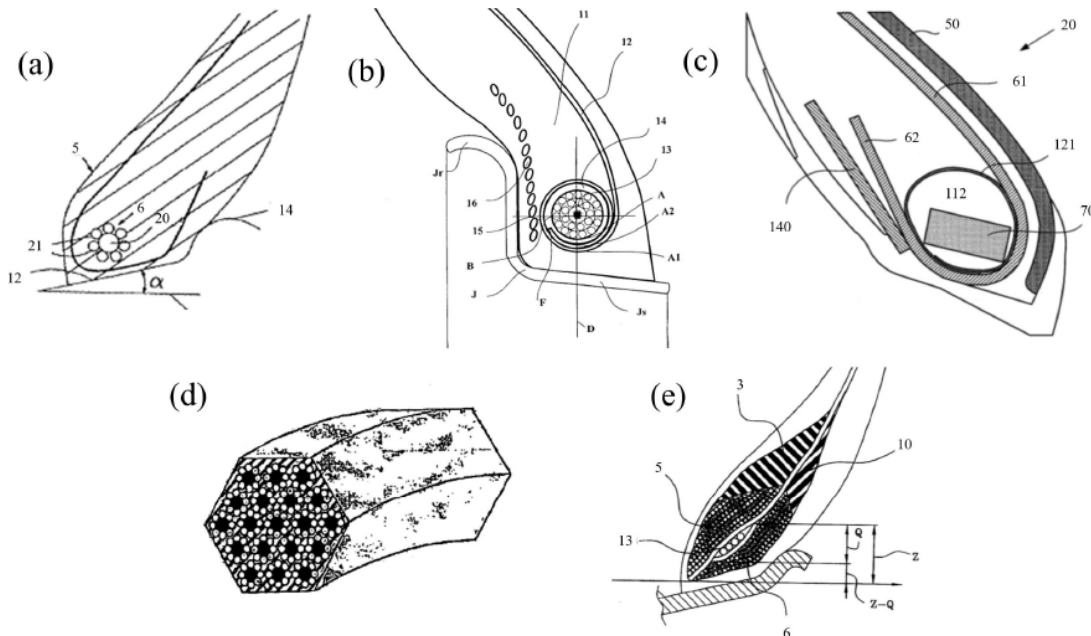


Figure 4: Various new steel bead structures: (a) Pirelli shape memory alloy bead; (b) Michelin rolled bead; (c) Michelin buffer rubber bead; (d) Compound bead of Pirelli Company; (e) Endurance enhances bead structure [11].

ring coated layer to enhance the tire cord layer's stability in the bead area. (c) buffer rubber tire bead: the tire ring is set between the tire ring and the tire cord layer of the rubber material buffer layer in order to reduce the relative slip of the original contact surface and enhance the tension concentration of the carcass cord.

These techniques illustrate the development trend of tire bead structure, which is to decrease the tension concentration on the tire cord and increase the tire's durability. Increase the torsional and bending rigidity of the bead to reduce relative displacement in the bead area and enhance the performance of the tire and rim assembly. Despite the fact that the aforementioned scholars have attempted to optimize the structure of the bead and that various institutions have proposed new bead structures, the research on the optimization design of the bead structure has yet to break out of the limitations of the bead wire, and various schemes continue to use the traditional wire bead, which has a number of limitations and flaws, and no new bead structure form has been proposed. Due to the traditional steel wire bead's composition of composite materials, its stress distribution is complex, it is prone to aging, and it is difficult to acquire the tire bead's fine shape due to the steel wire's geometric parameters. In order to further enhance the performance of the tire, the existing tire bead structure was optimized, and a new type of tire bead structure was proposed, which is anticipated to become the standard in the future.

In response to the geometrical limitation of steel wire beads for fine structural optimization, Li *et al.* [12] designed a whole bead structure as depicted in Figure 5. The von Mises stress with this structure is significantly lower at the outer end point of the chafer and the end point of the carcass cord than with the steel wire bead, and the face contact shape of the whole bead is more regular and the pressure distribution is more uniform. On the basis of the foregoing, the entire bead structure can provide enhanced performance and has vast application potential for ensuring tire availability and vehicle safety.

This novel structure has broad application potential for enhancing tire performance and vehicle security. However, the whole bead proposed based on experience lacks theoretical guidance and a scientific method of optimization. As a result, there are numerous stress concentrations in the inner side of the bead area, and it is crucial to find a scientific and reasonable method to optimize the design of the whole bead, which can effectively compensate for the flaws of the empirical design and further improve the performance of the tire under the load. It is essential to further enhance the performance of the tire under actual operating conditions, enhance the vehicle's driving performance, and ensure the driver's safety. The purpose of this paper is to optimize the topology of the traditional 265/35R18 semi-steel radial tire bead structure after its integration in order to further enhance

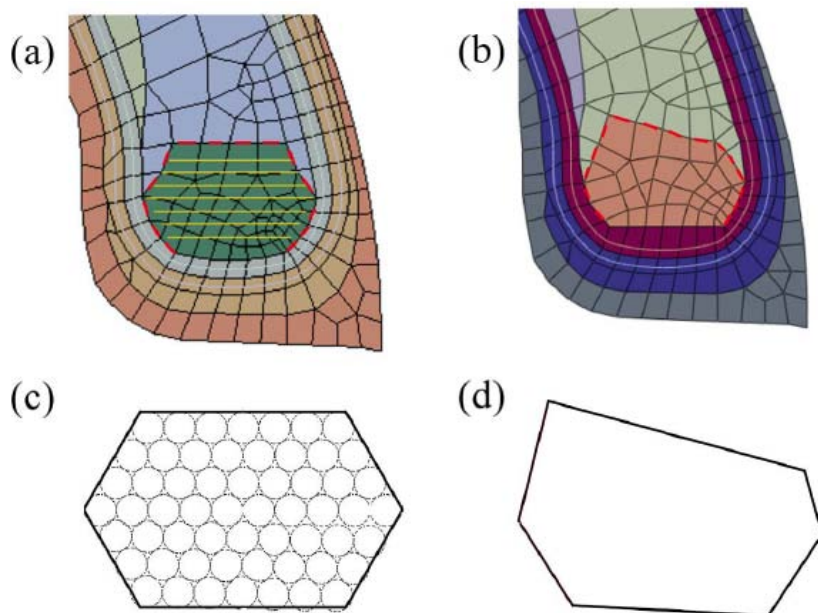


Figure 5: Concept design of the whole bead: (a) finite element model of steel wire bead; (b) finite element model of whole bead; (c) Schematic diagram of the structure of the wire bead; (d) Schematic diagram of the whole bead structure [12].

the tire's performance under actual charging conditions.

2. FAILURE MECHANISM OF TIRE COMPOSITE MATERIALS

2.1. Progressive Failure Model of Composite Materials

In 1980, Hashin studied the damage of fiber reinforced composites, and proposed a failure criterion to predict the failure state of composites in three-dimensional state. According to the geometric characteristics of the two-dimensional axisymmetric tire cross-section model, the Hashin failure model in three-dimensional state is transformed into a two-dimensional failure model, which is expressed as follows [13]:

- (1) Failure mode of matrix compression morphology, when $\sigma_{22} < 0$:

$$F_{mc} = \left[\left(\frac{Y_c}{2S_{23}} \right)^2 - 1 \right] \frac{\sigma_{22}}{Y_c} + \left(\frac{\sigma_{22}}{2S_{23}} \right)^2 + \frac{\sigma_{12}^2}{S_{12}^2} = 1 \quad (1)$$

- (2) Failure mode of matrix tensile morphology, when $\sigma_{22} \geq 0$:

$$F_{mt} = \frac{(\sigma_{22})^2}{Y_t^2} + \frac{\sigma_{12}^2}{S_{12}^2} = 1 \quad (2)$$

- (3) Fiber compression morphology failure mode, when $\sigma_{11} < 0$:

$$F_{fc} = \left(\frac{\sigma_{11}}{X_c} \right)^2 = 1 \quad (3)$$

- (4) Fiber tensile morphology failure mode, when $\sigma_{11} \geq 0$:

$$F_{ft} = \frac{\sigma_{11}^2}{X_t^2} + \alpha_s \left(\frac{\sigma_{12}^2}{S_{12}^2} \right) = 1 \quad (4)$$

The main function of the Hashin failure model in the two-dimensional state is to judge the starting point of material damage. In the failure mode of fiber tensile morphology, when the value is 1, it means that the composite material has a damage point in the tensile direction of the fiber. The failure model can be used as a more accurate failure criterion in finite element simulation to predict the damage failure of composite materials in the two-dimensional axisymmetric tire model.

2.2. Principle of Energy Damage Evolution of Composite Materials

In the process of failure assessment of laminated composite materials, there are generally five single stress states, as shown in Figure 6, namely: longitudinal tensile stress when fiber breaks; longitudinal compressive stress during fiber kink or instability; transverse tensile stress when the matrix is broken; transverse compressive stress during matrix shearing; and shear stress at macroscopic shear failure. These five stress states, longitudinal elastic modulus E_1 , transverse elastic modulus E_2 , shear modulus G_{12} and Poisson's ratio of composite materials ν_{12} are nine constants commonly used in engineering calculations [14].

After the structure is damaged, the stiffness of the composite material will gradually degrade with the increase of damage. At this time, the composite material is in the stage of damage evolution. In the following relationship, a variable d is used to describe the degradation state of the stiffness of the composite material in this stage of damage:

$$\sigma = C_0(d)\varepsilon \quad (5)$$

$$C_0(d) = \begin{bmatrix} (1-d_f)E_1 & (1-d_f)(1-d_m)\nu_{21}E_1 & 0 \\ (1-d_f)(1-d_m)\nu_{12}E_2 & (1-d_m)E_2 & 0 \\ 0 & 0 & (1-d_s)G_{12} \end{bmatrix} \quad (6)$$

Where d_s is shear damage variable; d_f is longitudinal fiber variable damage; d_m is the transverse matrix damage variable.

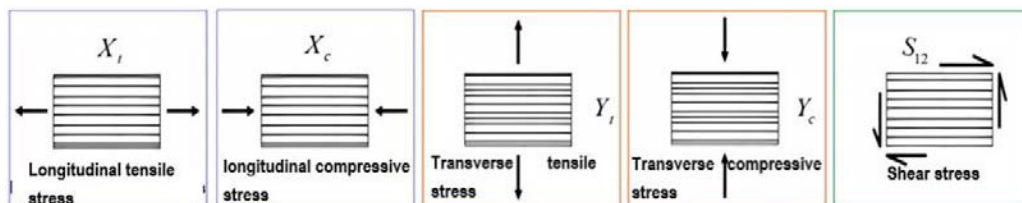


Figure 6: Stress state diagram of laminated composite structure.

Under normal conditions, in the damage evolution stage, the laminated composite material undergoes tensile or compressive damage in the longitudinal or transverse direction. When the longitudinal stress $\sigma_{11} \geq 0$, the material is in the tensile state $d_f = d_{ft}$, $\sigma_{11} \leq 0$, and the material is in the compressive state $d_f = d_{fc}$. The damage degree of the material d_f is described by a specific value between 0-1. Figure 7 shows the relationship between damage variables.

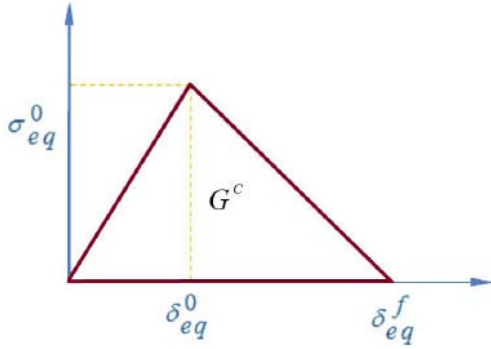


Figure 7: Principle of damage state variable.

After the tensile or compressive damage of the composite material, whether it is fiber damage or matrix damage, the shear capacity of the material in the damaged state is almost zero, which means that the shear damage variable d_s is closely related to the four damage variables d_{ft} , d_{fc} , d_{mt} and d_{mc} , in the horizontal and vertical directions. When any of these four variables is 1, that is, when the material completely fails in the state described by the variable, d_s is also [15].

$$d = \frac{\delta_{eq}^f (\delta_{eq} - \delta_{eq}^0)}{\delta_{eq} (\delta_{eq}^f - \delta_{eq}^0)} \quad (7)$$

Where δ_{eq} is equivalent displacement; σ_{eq} is equivalent stress; δ_{eq}^0 is the initial equivalent displacement of composite material damage; σ_{eq}^0 is the initial equivalent stress when the composite material is damaged; δ_{eq}^f is the equivalent displacement when the composite material is completely damaged.

In the process of finite element analysis and calculation, the relationship between equivalent stress and displacement under four failure modes can be described by the following relationship. Fiber tensile mode (8); Fiber compression mode (9); Matrix tensile mode (10); Matrix compression mode (11):

$$\delta_{eq}^{ft} = L^C \sqrt{\langle \varepsilon_{11} \rangle^2 + \alpha \varepsilon_{12}^2} \quad \sigma_{eq}^{ft} = \frac{\langle \sigma_{11} \rangle \langle \varepsilon_{11} \rangle + \alpha \tau_{12} \varepsilon_{12}}{\delta_{eq}^{ft} / L^C} \quad \sigma_{11} \geq 0 \quad (8)$$

$$\delta_{eq}^{fc} = L^C \langle -\varepsilon_{11} \rangle \quad \sigma_{eq}^{fc} = \frac{\langle -\sigma_{11} \rangle \langle -\varepsilon_{11} \rangle}{\delta_{eq}^{fc} / L^C} \quad \sigma_{11} < 0 \quad (9)$$

$$\delta_{eq}^{mt} = L^C \sqrt{\langle \varepsilon_{22} \rangle^2 + \varepsilon_{12}^2} \quad \sigma_{eq}^{mt} = \frac{\langle \sigma_{22} \rangle \langle \varepsilon_{22} \rangle + \tau_{12} \varepsilon_{12}}{\delta_{eq}^{mt} / L^C} \quad \sigma_{22} \geq 0 \quad (10)$$

$$\delta_{eq}^{mc} = L^C \sqrt{\langle -\varepsilon_{22} \rangle^2 + \varepsilon_{12}^2} \quad \sigma_{eq}^{mc} = \frac{\langle -\sigma_{22} \rangle \langle -\varepsilon_{22} \rangle + \tau_{12} \varepsilon_{12}}{\delta_{eq}^{mc} / L^C} \quad \sigma_{22} < 0 \quad (11)$$

Where L^C is the characteristic length of the composite material analysis unit.

According to the formula (8), (9), (10), (11), combined with the failure criterion of composite materials (4), (2), (1), with the increase of load, the damage initial displacement and equivalent stress expression of each material point under each failure mode can be obtained:

$$\begin{cases} \delta_{eq}^{0,ft} = \delta_{eq}^{ft} \Big|_{F_{ft}=1} & \sigma_{eq}^{0,ft} = \sigma_{eq}^{ft} \Big|_{F_{ft}=1} \\ \delta_{eq}^{0,fc} = \delta_{eq}^{fc} \Big|_{F_{fc}=1} & \sigma_{eq}^{0,fc} = \sigma_{eq}^{fc} \Big|_{F_{fc}=1} \\ \delta_{eq}^{0,mt} = \delta_{eq}^{mt} \Big|_{F_{mt}=1} & \sigma_{eq}^{0,mt} = \sigma_{eq}^{mt} \Big|_{F_{mt}=1} \\ \delta_{eq}^{0,mc} = \delta_{eq}^{mc} \Big|_{F_{mc}=1} & \sigma_{eq}^{0,mc} = \sigma_{eq}^{mc} \Big|_{F_{mc}=1} \end{cases} \quad (12)$$

Combined with the failure displacement expression:

$$\delta_{eq}^f = \frac{2G^c}{\sigma_{eq}^0} \quad (13)$$

Where G^c is critical strain energy release rate, that is, the fracture energy in the damage evolution stage, which describes the energy required for crack expansion per unit area during crack propagation. It can be divided into four types: longitudinal fiber tensile direction fracture energy G_{ftc} ; fracture energy in tensile direction of transverse matrix G_{mtc} ; longitudinal fiber compression direction fracture energy G_{fcc} ; fracture energy in transverse matrix compression direction G_{mcc} .

The damage variables of composite materials in four independent states can be obtained:

$$\left\{ \begin{aligned} \delta_{eq}^{f,ft} &= \frac{2G_{ft}^c}{\sigma_{eq}^{0,ft}} \quad d_{ft} = \frac{\delta_{eq}^{f,ft} (\delta_{eq} - \delta_{eq}^{0,ft})}{\delta_{eq} (\delta_{eq}^{f,ft} - \delta_{eq}^{0,ft})} \quad \delta_{eq}^{f,fc} = \frac{2G_{fc}^c}{\sigma_{eq}^{0,fc}} \\ d_{fc} &= \frac{\delta_{eq}^{f,fc} (\delta_{eq} - \delta_{eq}^{0,fc})}{\delta_{eq} (\delta_{eq}^{f,fc} - \delta_{eq}^{0,fc})} \\ \delta_{eq}^{f,mt} &= \frac{2G_{mt}^c}{\sigma_{eq}^{0,mt}} \quad d_{mt} = \frac{\delta_{eq}^{f,mt} (\delta_{eq} - \delta_{eq}^{0,mt})}{\delta_{eq} (\delta_{eq}^{f,mt} - \delta_{eq}^{0,mt})} \quad \delta_{eq}^{f,mc} = \frac{2G_{mc}^c}{\sigma_{eq}^{0,mc}} \\ d_{mc} &= \frac{\delta_{eq}^{f,mc} (\delta_{eq} - \delta_{eq}^{0,mc})}{\delta_{eq} (\delta_{eq}^{f,mc} - \delta_{eq}^{0,mc})} \end{aligned} \right. \quad (14)$$

According to the obtained damage state variable back to formula (5), the stress-strain relationship under the damage state can be obtained.

3. TOPOLOGY SHAPE OPTIMIZATION PRINCIPLE

3.1. Shape Optimization Method

As an optimization method to meet the structural performance requirements by adjusting the stress distribution, in most cases, the shape optimization is used for the final improvement of the determined structure in the design process, and the structure obtained by other design methods is further improved. On the basis of maintaining the overall layout of the structural components, according to the stress distribution obtained by the finite element analysis, the surface element nodes in the design area are adjusted by a small displacement to improve the effect of stress concentration and obtain a better structural design scheme. Based on the general description of the shape optimization problem, the boundary change problem can be described by the following formula [16]:

$$F^*[\Gamma_{var}^*(x)] = \min_{\Gamma_{var}} \{ F[\Gamma_{var}(x)] | \Gamma_{var}(x) \in \Omega \} \quad (15)$$

The shape optimization can be expressed as follows [17]:

$$\left\{ \begin{aligned} F^*[\Gamma_{var}^*(x)] &= \min_{\Gamma_{var}} \{ F[\Gamma_{var}(x)] | \Gamma_{var}(x) \in \Omega \} \\ \min : X(x) &= X(x_1, x_2, x_3, \dots, x_n) \\ \text{s.t.} : g_j(x) &\leq 0 \quad j = 1, \dots, m \\ h_e(x) &\leq 0 \quad e = 1, \dots, m \\ 0 \leq x_{\min} \leq x_i &\leq 1 \quad i = (1, 2, \dots, n) \end{aligned} \right. \quad (16)$$

Where F^* is the best shape design; F is design for shape; x is the design variables; x_i is a single design variable; Ω is the design area; $X(x)$ is the

objective function; $\Gamma_{var}(x)$ is design the structural boundary; $\Gamma_{var}^*(x)$ is the best structural boundary; $g_j(x)$ and $h_k(x)$ is the design response limited by added constraints.

3.2. Topology Optimization Method

It is assumed that in the process of topology optimization design, the bead structure of the tire is regarded as a static linear elastic structure with minimum stiffness topology design under a single load condition. This design is equivalent to the minimum flexibility design. The minimum flexibility is defined as the work done by a set of given loads on the equilibrium displacement. Then the design process can be regarded as minimizing the total elastic energy in the equilibrium state of the structure [18]. The topology optimization problem in this process can be described as a problem of designing distributed discrete values, that is, 0-1 problem. In order to solve this problem, a density variable is introduced, whose value varies between 0 and 1, representing the degree of existence of the material. When the density value is 0, the corresponding material does not exist; when the density value is 1, it means that the material exists completely. Then assuming that the objective of topology optimization is to minimize the volume of the structure, the density properties of the material and the elastic modulus values have the following relationship [19]:

$$E(x_i) = E_{\min} + x_i(E_0 - E_{\min}) \quad x_i \in [0, 1] \quad (17)$$

Where x_i is a single design variable, namely the density of the i unit; $E(x_i)$ is the elastic modulus of the material for the i element; E_0 is the elastic modulus of the unit material; E_{\min} is the elastic modulus when the unit material does not exist.

In order to prevent the singular problem of the stiffness matrix from being solved, it can be made $E_{\min} = E_0 / 1000$. At the same time, in order to avoid the problem that there is no non-0 or 1 density elements in the structure during the optimization process, a penalty interpolation function can be set. In this method, a power function is used as the penalty function, and the density penalty of all elements is classified to 0 or 1, so as to eliminate the intermediate density element and solve the problem that the actual structure has no intermediate density element. The SIMP method can be described by the following expression [20]:

$$\begin{cases} f(x_i) = x_i^{p^*} \\ x_i \in [0, 1], i = (1, 2, \dots, n) \end{cases} \quad (18)$$

Where p^* is the penalty factor.

The introduced structural stiffness and strain energy are as follows:

$$\begin{cases} E(x_i) = E_{\min} + x_i(E_0 - E_{\min}) & x_i \in [0, 1] \\ \mathbf{K} = \sum_{i=1}^n (E_{\min} + x_i^{p^*} \Delta E) \mathbf{k}_i \\ U^e = \frac{1}{2} \mathbf{r}^{*T} \mathbf{d}^* = \frac{1}{2} \mathbf{d}^{*T} \mathbf{K} \mathbf{d}^* = \sum_{i=1}^n \frac{1}{2} (E_{\min} + x_i^{p^*} \Delta E) \mathbf{d}_i^{*T} k_i \mathbf{d}_i^* \end{cases} \quad (19)$$

Where \mathbf{d}^* is the displacement vector; \mathbf{K} is the stiffness matrix; \mathbf{r}^* is a load vector; U^e is strain energy; k_i is element stiffness; x_i is design variables, represents the unit density.

The initial bead structure often does not conform to the processing technology specification, and considering the actual working conditions and safety problems of the tire, the initial structure often has unreasonable concave and convex boundaries or sharp corners. Therefore, the whole bead structure needs to be further refined and smoothed after the topology and initial boundary shape are determined. The local gradient mesh smoothing algorithm is selected, which will identify the elements with the worst quality and improve by replacing the nodes. Finally, the mathematical model of variable density topology shape optimization based on the SIMP interpolation model is as follows:

$$\begin{cases} F^*[\Gamma_{var}^*(x)] = \min_{\Gamma_{var}^*(x)} \{F[\Gamma_{var}^*(x)] | \Gamma_{var}^*(x) \in \Omega\} \\ B = \left\{ X \mid \int_{\Omega} X dx = V_{\text{fixed}} \right\} \\ \min : U^e(x) = \sum_{i=1}^n (E_{\min} + x_i^{p^*} \Delta E) \mathbf{d}_i^{*T} k_i \mathbf{d}_i^* \\ s.t. : \sum_{i=1}^n x_i v_i - V^* \leq 0 \\ \mathbf{K} \mathbf{d}^* = \mathbf{r}^* \\ 0 \leq x_{\min} \leq x_i \leq 1 \quad i = (1, 2, \dots, n) \end{cases} \quad (20)$$

Where B is best topology design; F^* is the design for the best shape; F is the design for shape; p^* is the penalty factor; x_i is the design variable,

representing the unit density; d_i is the unit displacement; k_i is the element stiffness; v_i is the initial volume of each unit; V^* is the overall volume constraint of the structure; $\Gamma_{var}^*(x)$ is the structure boundary is the bead boundary; $\Gamma_{var}^*(x)$ is the best structural boundary.

4. TOPOLOGY SHAPE OPTIMIZATION CRITERIA

4.1. Von Mises Optimization Criterion

At present, the optimization of tires [21, 22] mostly uses Von-Mises stress as the main optimization criterion. The criterion mainly considers the yield effect of principal stress on the material, and the damage occurs when the deformation energy reaches the energy required for the material yield failure. The tire cord layer is a composite material of rubber and cord, which will inevitably produce interlaminar shear stress when subjected to the transverse load. Only considering the Von-Mises stress has certain limitations, but as a commonly used material yield criterion, it considers the influence of intermediate principal stress on the material. The von-Mises criterion requires fewer material parameters, which can be measured experimentally. The expression is [23]:

$$J_2 - k_2^2 = 0 \quad (21)$$

Where σ_s is the initial yield stress of the material; J_2 is the second invariant of stress partial tensor; k_2 is the material constants for the von-Mises yield criterion can be determined by tensile or pure shear tests:

$$k_2 = \frac{\sigma_s}{\sqrt{3}} = \tau_s \quad (22)$$

This means that when the von Mises criterion is used, the yield condition of the default material satisfies $\sigma_s = \sqrt{3} \tau_s$. In the principal stress space, the yield surface of the Mises criterion is a cylindrical surface and is perpendicular to the π plane. The expression is:

$$\sqrt{J_2} - \frac{1+\nu}{E} c = 0 \quad (23)$$

Where E is the elastic modulus; ν is the Poisson's ratio of the material; C is the cohesion of the material.

The von-Mises equivalent stress in the finite element analysis software can be expressed as follows [24]:

$$\begin{cases} \mathbf{S}_{ij} = \sigma_{ij} + p\delta_{ij} \\ p = -\frac{1}{3}\sigma_{ij} \end{cases} \quad (24)$$

Where \mathbf{S}_{ij} is the deviatoric stress tensor; p is equivalent compressive stress; δ_{ij} is the deviatoric stress tensor reflecting the change of plastic deformation shape.

4.2. Generalized Drucker-Prager Optimization Criterion

In 1952, Drucker and Prager proposed a yield criterion suitable for geotechnical materials. The supplementary von-Mises criterion cannot consider the influence of hydrostatic pressure on material failure, namely the D-P strength criterion. The expression of the criterion is as follows [25]:

$$\sqrt{J_2} - \alpha I_1 = k \quad (25)$$

Usually, the above formula is called the D-P series yield criterion. When $\alpha = 0$, it is the von-Mises criterion. Since the D-P strength criterion has some defects from the energy point of view, Guo Jianqiang *et al.* proposed the generalized D-P strength criterion. Its physical meaning is: according to the energy conservation in the physical process, where U is the total energy, U^e is the elastic strain energy, and U^d is the dissipation energy, which satisfies the law of thermodynamics. Without defining the Poisson's ratio of 0.5, when the elastic strain energy U^e is critical, the material begins to yield and fail [26]:

$$\begin{cases} U = U^d + U^e \\ = U^d + U^{el_1} + U^{el_2} \\ = \int_0^{\epsilon_1} \sigma_1 d\epsilon + \int_0^{\epsilon_2} \sigma_2 d\epsilon + \int_0^{\epsilon_3} \sigma_3 d\epsilon \\ U^e = \frac{1}{2E} [\sigma_1^2 + \sigma_2^2 + \sigma_3^2 - 2\nu(\sigma_1\sigma_2 + \sigma_1\sigma_3 + \sigma_2\sigma_3)] \\ = \frac{3}{2E} \left(J_2 - \frac{1-2\nu}{3} I_2 \right) \end{cases} \quad (26)$$

According to the D-P criterion expression (25):

$$\sqrt{\frac{3}{2E} J_2} = \sqrt{\frac{3}{2E}} (k + \alpha I_1) \quad (27)$$

According to the (26):

$$\sqrt{U^e} = \sqrt{\frac{3}{2E} \left(J_2 - \frac{1-2\nu}{3} I_2 \right)} \quad (28)$$

Because $\nu = 0.5$ is defined in the generalized D-P strength assumption, that is, the ultimate Poisson's ratio of elastic-plastic materials in the ideal state, then Eq. (27) can be expressed as :

$$\begin{aligned} \sqrt{U^e} &= \sqrt{\frac{3}{2E} \left(J_2 - \frac{1-2*0.5}{3} I_2 \right)} \\ &= \sqrt{\frac{3}{2E} \left(J_2 - \frac{1-2\nu}{3} I_2 \right)} = \sqrt{\frac{3}{2E}} (k + \alpha I_1) \end{aligned} \quad (29)$$

The generalized D-P strength criterion is described by elastic strain energy:

$$\begin{cases} \sqrt{\frac{2E}{3} U^e} = \sqrt{\left(J_2 - \frac{1-2\nu}{3} I_2 \right)} = k + \alpha I_1 \\ \sqrt{\left(J_2 - \frac{1-2\nu}{3} I_2 \right)} - \alpha I_1 = k \end{cases} \quad (30)$$

Introducing the D-P criterion in the optimization design:

$$k = \frac{\left\{ \frac{\nu-1}{2\nu} + \frac{1+\nu}{2\nu} (\sigma_1 + \sigma_2 + \sigma_3) \right\}}{\sqrt{\frac{1}{2} (\sigma_1 - \sigma_2)^2 + (\sigma_2 - \sigma_3)^2 + (\sigma_3 - \sigma_1)^2}} \quad (31)$$

In the form of the first stress invariant and the second stress invariant of the stress deviation (30), the stress invariant expression using the D-P hypothesis in the optimization process is obtained:

$$\left(\frac{\nu-1}{2\nu} + \frac{1+\nu}{2\nu} I_1 \right) \sqrt{3J_2} - \sqrt{\left(J_2 - \frac{1-2\nu}{3} I_2 \right)} + \alpha I_1 = 0 \quad (32)$$

In the process of optimization iteration, the generalized D-P strength criterion expressed by elastic strain energy is corresponding to the D-P criterion in optimization design. In the process of optimization design, not only the influence of structural form on stress is considered, but also the influence of the change of structural properties of the whole composite material in the process of damage evolution is considered.

4.3. Tresca Optimization Criterion

In the process of damage evolution of composite materials [27], although the engineering constants of rubber and steel cord will not change, the properties of the composite structure will change with the damage. Therefore, the structural properties of composite

materials should be considered in the optimization process. The Von-Mises stress and interlaminar shear stress of the rubber element near the end of the cord are selected as the main criteria for structural optimization, and the Tresca hypothesis is introduced to explain the specific application of interlaminar shear stress in the finite element analysis process.

The Tresca hypothesis [28] means that the material satisfies the following conditions:

$$\tau_s = 2\sigma_s \quad (33)$$

When the magnitude of the principal stress is unknown, the Tresca yield condition is not easy to apply. In addition, the Tresca yield condition ignores the influence of intermediate principal stress, and there is a corner on the yield line, which brings difficulties to mathematical processing. In general, it is impossible to determine the magnitude of the three principal stresses at each point in the solid in advance [29]. Therefore, the condition should be expressed by the following function in finite element analysis:

$$\text{MAX}[\sigma_1 - \sigma_2, \sigma_2 - \sigma_3, \sigma_1 - \sigma_3] / 2 = \tau_s \quad (34)$$

Combined with interlaminar shear stress based on composite materials [30]:

$$\tau = \frac{E_a E_b (v_b - v_a) \lambda \sigma_0}{(E_a + E_b k) \left(E_a \frac{1}{k} + E_b \right)} \quad (35)$$

It can be concluded that the composite material of rubber and cord in the carcass cord layer can be expressed by the following formula, that is, the reason for the failure of the tire under the assumption of maximum shear stress is only related to the ratio of the thickness of the rubber material to the thickness of the cord material in the composite unit and the thickness-width ratio of the unit on the compression surface under the condition that the material property constant is constant.

$$\begin{aligned} & \text{MAX}[\sigma_1 - \sigma_2, \sigma_2 - \sigma_3, \sigma_1 - \sigma_3] / 2 \\ &= \frac{E_a E_b (v_b - v_a) \lambda \sigma_0}{(E_a + E_b k) \left(E_a \frac{1}{k} + E_b \right)} \end{aligned} \quad (36)$$

Where E_a and E_b are rubber and cord elastic modulus; ε_a and ε_b are free strain caused by Poisson

's ratio effect is not considered; v_a is poisson's ratio of rubber material; v_b is poisson's ratio of cord material; τ is interlaminar shear stress; k is the ratio of rubber material thickness to cord material thickness in composite material unit; λ is thickness-width ratio of the element on the compression surface.

5. ESTABLISHMENT OF FINITE ELEMENT ANALYSIS MODEL

5.1. Material Constitutive Model

Yeoh model is a subtype of reduced polynomial with N equal to 3. Since rubber cannot be compressed under normal conditions, it is presumed that the rubber's volume does not change during deformation and that only its geometric shape changes; therefore, Yeoh can be expressed as [31]:

$$U^e = \sum_{i=1}^3 C_{i0} (I_1 - 3)^i \quad (37)$$

Where C_i is Yeoh model material parameters.

Yeoh model is a common strain energy function applicable to a wide range of deformations and capable of precisely describing the material's behavior under complex conditions. The coefficient of the Yeoh model can be determined by a uniaxial tensile test, which is characterized by a straightforward experiment and high calculation accuracy [32]. Taking into account the experiment and calculation precision requirements, this paper intends to employ the Yeoh model. The Yeoh model parameters of each rubber part in the tire are shown in Table 1.

5.2. Cord Reinforcement Model

For modeling purposes in finite element simulation analysis, the vulcanized tire shape is typically employed. Figure 8 depicts how the angle of the steel cord will shift slightly during the vulcanization process. This modification is most apparent on the semi-steel tire. During the calendaring operation of the belt or cord layer, the angle of the steel cord before vulcanization can be determined. To achieve a more precise setting of the steel cord's geometric structure, the vulcanization mapping equation is used to realize the geometric mapping from the structure to the vulcanized structure.

By specifying the spacing and angle of the steel cord before vulcanization, the cord spacing s and the

Table 1: Material Parameters of 265/35R18 Steel-belted Radial Tire Rubber

Material name	Density (kg/m ³)	Yoech model parameters of hyperelastic materials			
		C10	C20	C30	D1
Cap layer MRBT01	1137	0.8963	-0.4151	0.1684	0.02
Belt ply MRBT1/2	1191	1.0814	-0.4980	0.2282	0.02
Gas-tight layer MRNC	1254	0.5823	-0.3144	0.1209	0.02
Sidewall rubber MRNM	1175	1.3968	-1.6681	1.6213	0.02
Apex MRTA	1159	2.6813	-3.4637	3.5962	0.02
Shoulder rubber MRTC	1099	0.5991	-0.3146	0.1166	0.02
Tread rubber MRTM	1172	0.6556	-0.3457	0.1635	0.02
Somatogel MRTT1/2	1134	0.7206	-0.3381	0.1422	0.02

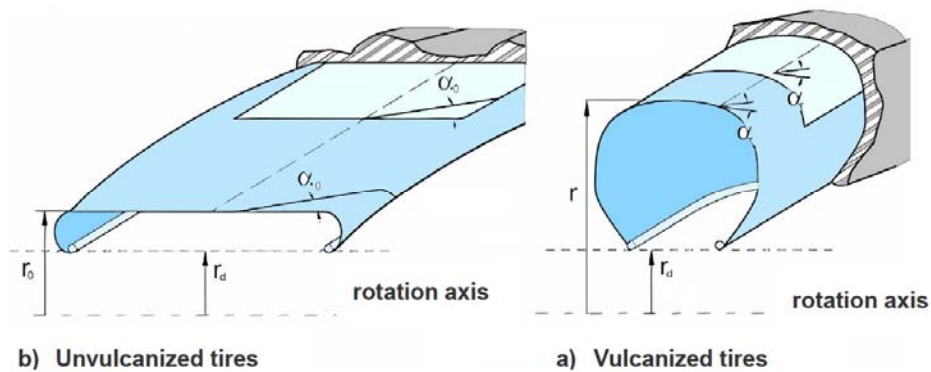


Figure 8: Geometric mapping of tire structure before and after vulcanization.

cord arrangement angle orientation α_v in the vulcanized tire can be mapped using the following equation:

$$\begin{cases} \sin \alpha_v = \frac{r \sin \alpha_0}{r_0(1 + e_r)} \\ s = s_0 \frac{r \cos \alpha_v}{r_0 \cos \alpha_0} \end{cases} \quad (38)$$

where r is the radial position of steel cord in the structure after vulcanization; s is the spacing of the cord after vulcanization; r_0 is the radial position of the steel cord in the unvulcanized structure; s_0 is the spacing in the unvulcanized structure; α_0 is the angle

projected in the local coordinate system relative to the unvulcanized structure; e_r is the angle of the vulcanization structure in the local coordinate system; for steel cord elongation, in the tire $e_r = 1$ represents 100 % extension. When α_0 equal to 90° , it is assumed that the reinforcement has a constant spacing s_0 .

5.3. Finite Element Modeling

Based on the optimization design of a 263-35R18 car tire with a traditional steel wire bead structure, the plane material structure drawing of the tire is drawn using two-dimensional drawing software, and the non-essential geometric structure is processed to reduce the complexity of model meshing at a later stage and

Table 2: Material Parameters of Steel Cord for 265/35R18 Radial Tire

Wire material	Density (kg/m ³)	Temperature (°C)	Young's modulus (MPa)	Poisson's ratio
MSBD	7800	25	110000	0.33
MSBT1	3960	25	93120	0.33
MSBT2	3960	25	93120	0.33

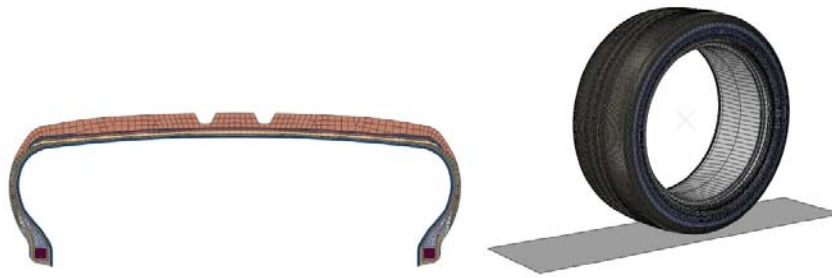


Figure 9: Original three-dimensional 265-35R18 model.

improve the convergence and calculation accuracy of finite element calculations. The cmd restart command can be used to transform a two-dimensional finite element analysis model into a three-dimensional model based on a two-dimensional finite element model. The finished model is depicted in Figure 9:

5.4. Accuracy Analysis of Finite Element Simulation Model

For the same purpose, the simulation and the actual experiment are investigated from the perspectives of virtuality and actuality. Due to the need to examine the same problem from two different perspectives, the two must complement one another, making the simulation model's precision crucial. To ensure the accuracy and dependability of the simulation optimization experiment, the company DOUBLESTAR assisted in carrying out the experiment depicted in Figure 10 involving the 8590.625 N radial load of a 265/35R18 tire. Simultaneously, the simulation experiment was conducted with the same radial load, and the radial rigidity data for both are displayed in Figure 11.

According to the tire load index (265/35R18:103/97-875kg/730kg), the specific working conditions are set as follows:

- (1) No-load conditions under the two-dimensional model: standard tire pressure $P=0.29\text{MPa}$, assembly pressure $P=0.01\text{MPa}$, and then the appearance size of inflation, cord stress at the bead area, rubber stress at the end of cord, and rim contact stress were compared and analyzed.
- (2) Load conditions under the three-dimensional model: the standard tire pressure $P=0.29\text{MPa}$ and the load $F=8600\text{N}$. Then, the cord stress at the bead area and the rubber stress at the end of the cord were compared and analyzed.
- (3) The torsion condition under the three-dimensional model: the standard pressure in the tire $P=0.29\text{MPa}$, the load $F=8600\text{N}$, and the static torsion Angle of 15° . On this basis, the impression analysis was carried out.

The radial load was gradually loaded from 0 to 8590.625N, and the 3D simulation experiment was

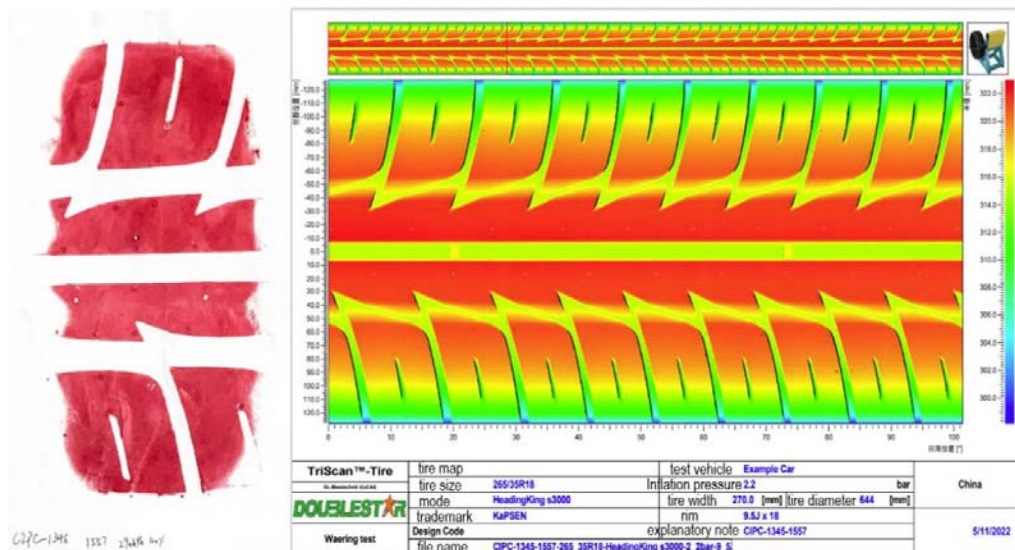


Figure 10: 265/32R18 tire footprint and tire surface scanning.

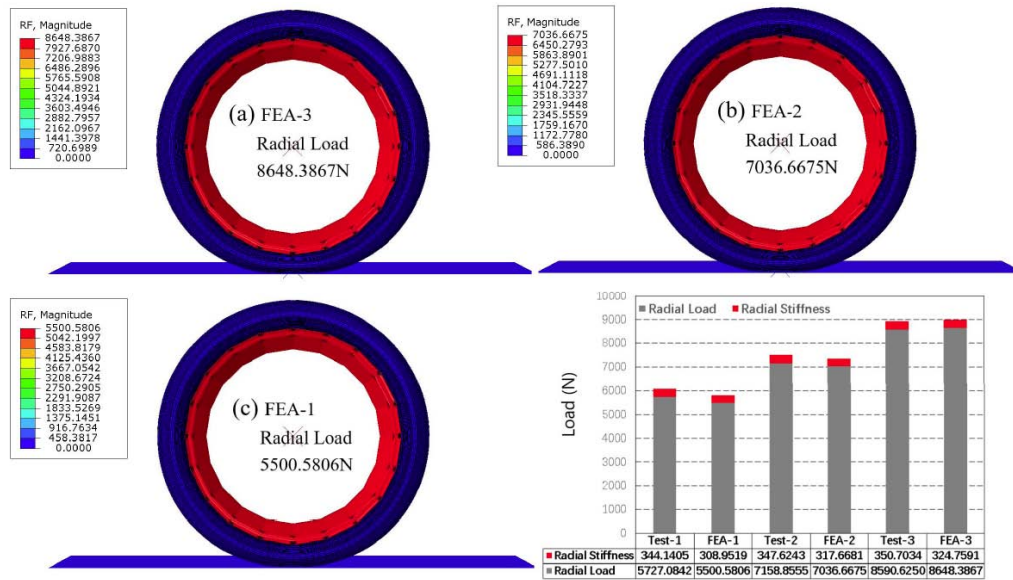


Figure 11: Comparison of 265/32R18 tire stiffness experiment and simulation.

conducted and compared with the actual experimental data, aiming to verify the accuracy of the 3D model in the simulation experiment. By comparing the experimental stiffness and simulation stiffness under the load conditions of 5500N, 7100N, and 8600N, the simulation errors were as follows: 10.22%, 8.61%, and 7.3%, verifying that the simulation model can more truly reflect the actual tire operation.

6. OPTIMIZATION DESIGN OF THE OVERALL BEAD TOPOLOGICAL SHAPE OF 265/35R18 SEMI-STEEL RADIAL TIRE

6.1. Empirical Design

In accordance with the development trend of steel wire bead and in pursuit of the quadrilateral bead

structure of the original 265/35R18 semi-steel radial automobile tire, an empirically designed hexagonal structure, as depicted in Figure 12, is proposed. After modeling with finite elements, a simulation experiment is conducted to determine whether the hexagonal structure's design is reasonable and practicable.

Based on the experience-designed hexagonal bead structure, Table 3 displays the simulation verification analysis data. Although the von Mises stress at the inner end of the chafer within the bead area increases, the von Mises stress at the outer end of the chafer at the bead part decreases by 31.55%, and the von Mises stress at the outer end of the carcass cord at the sub-mouth part decreases by 12.32%. Because the risk

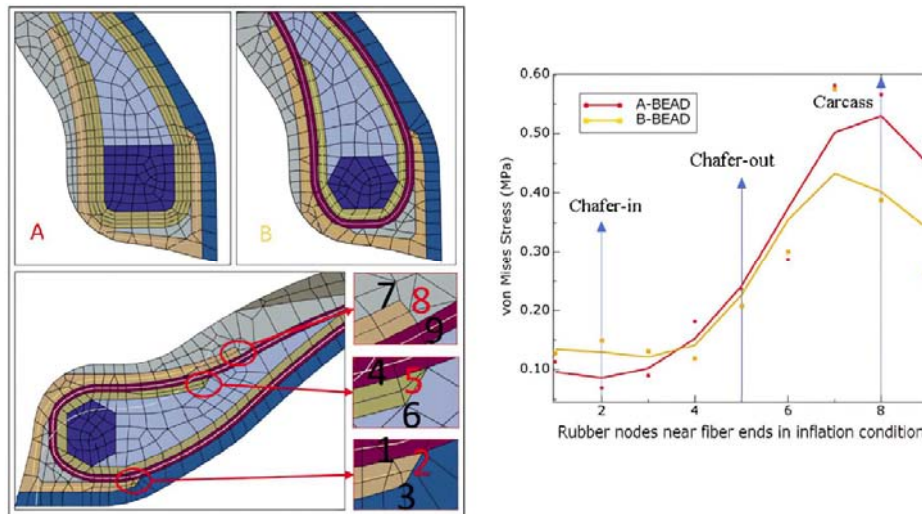


Figure 12: Comparison of von Mises stress between the inner and outer ends of the chafer cord and the outer end of the carcass cord in the bead area of the original 265/35R18 steel-belted radial tire structure A and hexagonal bead structure B.

Table 3: The Von Mises Optimization Value of Cord Endpoints at the Bead Area

von Mises	A/MPa	B/MPa	A-B/MPa	PCT
Chafer-in	0.0693	0.1493	-0.0800	-115.53%
Chafer-out	0.2368	0.2076	0.0292	12.32%
Carcass	0.5660	0.3874	0.1786	31.55%

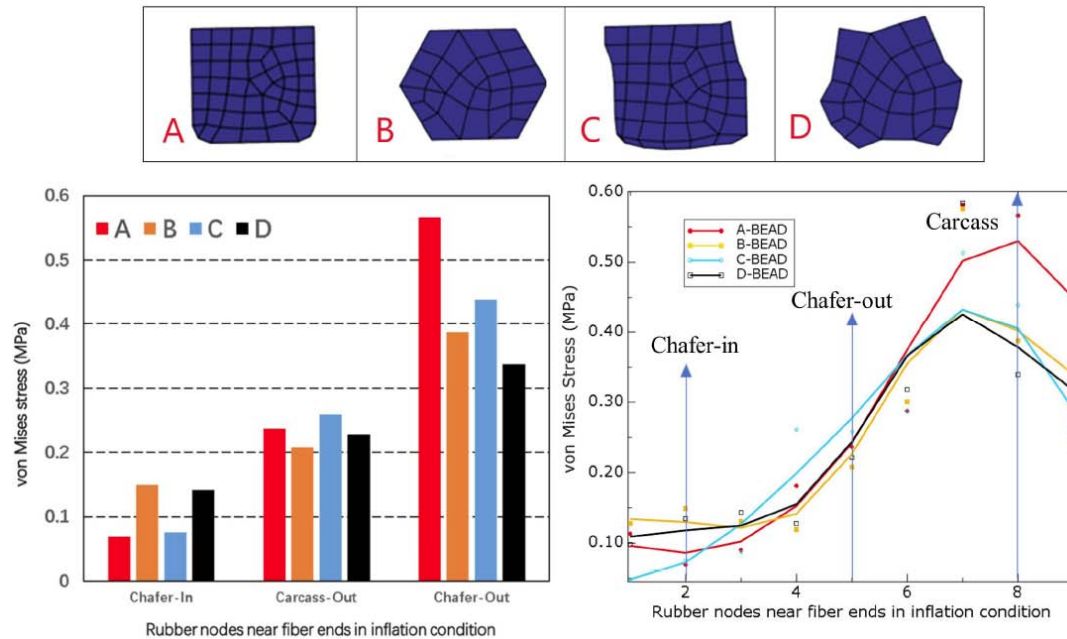


Figure 13: The von Mises stress analysis and comparison of the original quadrilateral bead A, hexagonal design bead B, optimized based on quadrilateral bead structure C, optimized based on hexagonal bead structure D at the cord endpoint in the bead area.

outside the bead area is significantly greater than that inside the bead area, the analysis demonstrates that the above empirical design can effectively improve the stress distribution at the bead area and reduce the harm at the bead area's outer end.

6.2. The Von Mises Stress of Cord and Cord End Points in the Support Area Was Optimized in A Single Design

Due to the absence of theoretical optimization, the singular empirical design lacks broad applicability and optimization capability. Consequently, based on the empirical design, the bead structure of 265-35R18 was optimized to enhance the tire's performance under actual working conditions. The initial objective of optimization is to minimize the von-Mises maximal value at the cord end and in the bead region. Without specifying boundary constraints, the von-Mises hypothesis is used as the primary optimization criterion to optimize the topological shape of the bead profile. A is the original 265/35R18 quadrilateral bead, B is the

empirically designed hexagonal bead, C is the direct optimization design of the original quadrilateral bead, and D is the optimization design of the empirically treated hexagonal bead, as illustrated in Figure 13.

6.2.1. Von Mises Optimization Check of Curtain End Points in the Bead Area

In the disease associated with the bead area, the proportion of damage occurring outside the bead is significantly greater than that occurring inside the bead, and the maximal stress at the end of the cord inside the bead is also significantly lower than that occurring outside the bead. Figure 13 depicts a comparison between the optimization result D based on the hexagonal bead B designed through experience and the direct optimization result C. Although the stress value within the bead area has increased, the von Mises stress outside the bead area, i.e., the outer end of the chafer and the outer end of the cadaver cord, has a positive effect on performance. Consequently, empirical design is utilized for the optimization design.

Table 4: Comparison of Von Mises Stress Between Empirical Design and Direct Optimization Design at the End of The Cord in the Bead Area

von Mises	A-B(MPa)	PCT	A-C(MPa)	PCT
Chafer-in	-0.0800	-115.53%	-0.0061	-8.87%
Chafer-out	0.0292	12.32%	-0.0218	-9.20%
Carcass-out	0.1786	31.55%	0.1270	22.44%

Table 5: After Optimized, the Comparison of Von Mises Stress of the Cord Endpoints in the Bead Area

von Mises	B-D(MPa)	PCT	A-D(MPa)	PCT
Chafer-in	0.0080	5.35%	-0.0720	-104.00%
Chafer-out	-0.0200	-9.62%	0.0092	3.89%
Carcass-out	0.0502	12.97%	0.2288	40.43%

It can shorten the optimization design cycle and improve optimization outcomes. The specific optimization outcomes are displayed in Tables 4 and 5 above.

The optimization results show a relatively excellent optimization effect. After the optimization of the bead structure of the hexagonal design, compared with the original quadrilateral structure, the von Mises stress at

the outer end of the carcass cord is reduced by 40.43%, and the von Mises stress at the outer end of the chafer is reduced by 3.89%.

6.2.2. Von Mises Optimization Check on Chafer Cord

The tire usually needs to set a chafer as a reinforcing and transition structure in the bead area to ensure that the tire is running in the vehicle, that is, in

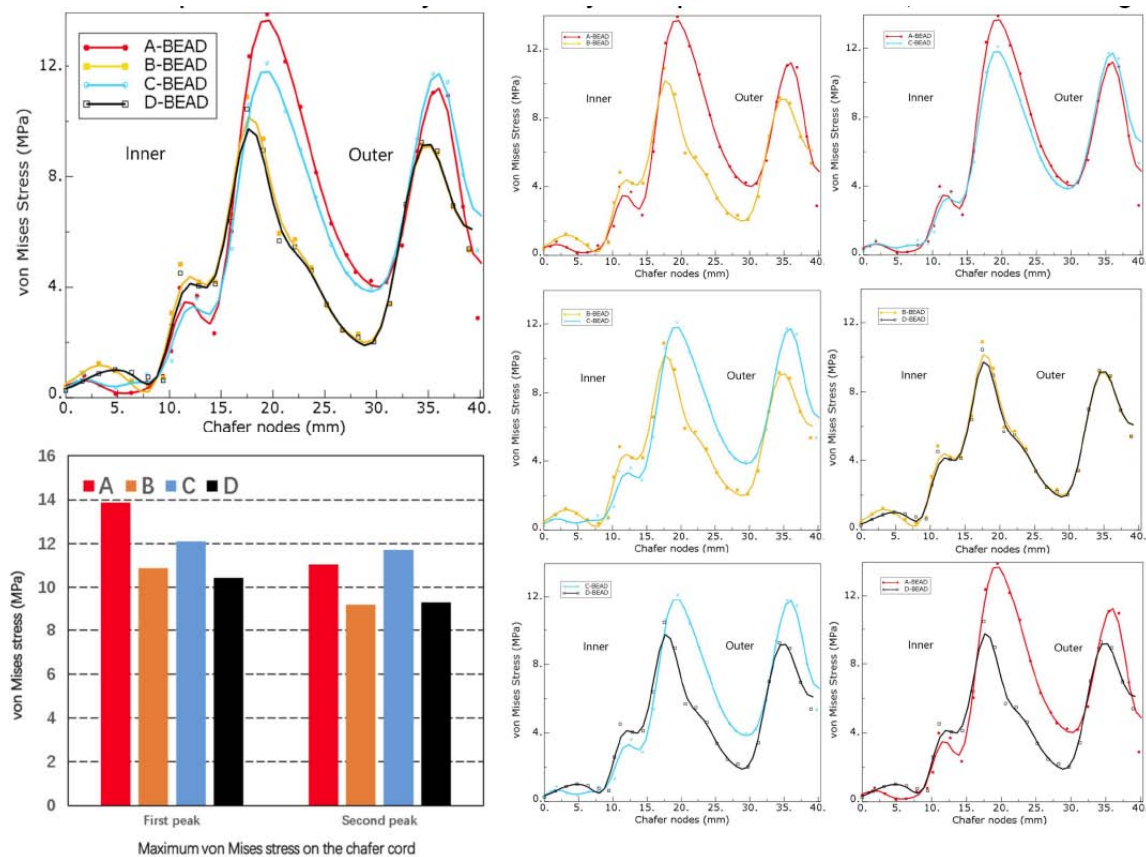


Figure 14: The von Mises stress analysis and comparison of the original quadrilateral bead A, hexagonal design bead B, optimized based on quadrilateral bead structure C, optimized based on hexagonal bead structure D on the chafer cord in the bead area.

Table 6: The Two Stress Peaks of Each Structure on the Chafer Cord at the Bead Area

Chafer cord	A(MPa)	B(MPa)	C(MPa)	D(MPa)
First peak	13.8691	10.8822	12.097	10.4374
Second peak	11.0424	9.17178	11.7221	9.25402

the actual working process of the bead area, the stability of the tire is maintained under a large load. Therefore, in the optimization process, it is necessary to pay attention to the stress concentration of the chafer cord. The von Mises stress on the chafer cord after one optimization is analyzed to verify the optimization effect, as shown in Figure 14.

As shown in Table 6, compared with the original structure A, the bead structure B has a good optimization effect on the two stress peaks at the contact position between the chafer and the rim and the outer position of the bead area, which proves that the empirical structure meets the design requirements. As shown in Tables 7 and 8, the first peak value of the optimized bead structure D is 4.09% higher than that of the B structure. Compared with the original bead structure A, the optimization effect of the first peak in the chafer reaches 24.74%, and the optimization effect of the second peak reaches 16.20%.

Since the single von Mises assumption is used as the criterion, the design response is the von Mises stress at the end of the cord and on the cord, and the objective function is to minimize the maximum stress. In this process, the main task of optimization is to reduce the maximum von Mises stress in the bead area. It is difficult to take into account that all the design response areas are positive optimization, so it will appear on the second peak. The direct optimization processes A to C and B to D are reverse negative

optimization. This process also reflects the importance of empirical design before using algorithm optimization.

6.2.3. Von Mises Optimization Check on Carcass Curtain Line

As the skeleton structure of the tire, the carcass cord has the risk of fracture due to stress concentration. Figure 15 below is the von Mises stress distribution of the carcass cord around each bead structure during the initial optimization process.

As shown in Tables 9 and 10, the structure B, in the position of the contact between the bead area and the rim (20-30mm), there is a stress concentration phenomenon that is not present. Structure C caused more obvious stress concentration in the outer region of the bead area. The above two designs have not reached the ideal design expectations. After considering other optimization evaluation indicators, when selecting an optimized design for the bead structure designed for experience, the purpose of reducing the carcass cord is to eliminate the von Mises stress concentration on the carcass cord at the contact position between the bead area and the rim. The von Mises stress on the carcass cord of the optimized bead structure D is shown in Figure 16.

As shown in Table 11, although the von Mises values of the optimized structures D and A at 34 mm of the data path increased by 1.36 MPa and the increase ratio reached 52.99%, they were still lower than the overall stress values on the cord. The final optimization

Table 7: Comparison of Von Mises Stress Between Empirical Design and Direct Optimization Design on the Chafer Cord in the Bead Area

Chafer cord	A-B(MPa)	PCT	A-C(MPa)	PCT
First peak	2.9869	21.54%	1.7721	12.78%
Second peak	1.8706	16.94%	-0.6797	-6.16%

Table 8: After Optimized, the Comparison of Von Mises Stress on the Chafer Cord in the Bead Area

Chafer cord	B-D(MPa)	PCT	A-D(MPa)	PCT
First peak	0.4448	4.09%	3.4317	24.74%
Second peak	-0.0822	-0.90%	1.7884	16.20%

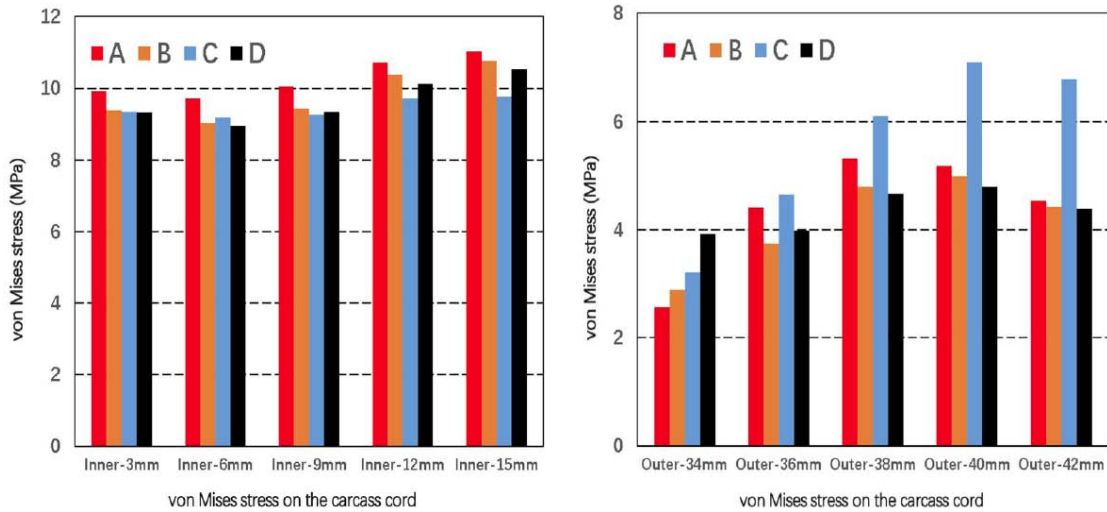


Figure 15: Comparison of von Mises stress concentration of each structure on the inner and outer carcass cords in the bead area.

Table 9: The Von Mises Stress Concentration on the Inner Carcass Cord in the Bead Area

Inner-path/mm	A(MPa)	B(MPa)	C(MPa)	D(MPa)
3	9.9102	9.3730	9.3406	9.3250
6	9.7311	9.0294	9.1887	8.9523
9	10.0439	9.4376	9.2702	9.3352
12	10.7251	10.3699	9.7309	10.1238
15	11.0353	10.7648	9.7714	10.5355

Table 10: The Von Mises Stress Concentration on the Outer Carcass Cord in the Bead Area

Outer-path/mm	A(MPa)	B(MPa)	C(MPa)	D(MPa)
34	2.5668	2.8827	3.1995	3.9269
36	4.4145	3.7507	4.6630	3.9993
38	5.3160	4.7942	6.0951	4.6683
40	5.1815	4.9923	7.1024	4.7926
42	4.5376	4.4281	6.7725	4.3852

effect, the original quadrilateral bead structure A and the structure D optimized based on empirical design, the optimization effect on the inner carcass cord of the bead area is 4.53% to 8%, and the optimization effect on the outer carcass cord of the bead area is 3.36% to 12.18%.

6.3. The Interlaminar Shear Stress of Cord Ends in the Bead Area Was Optimized For the Second Time

During the use of tires, under the action of thermal oxygen aging and interlaminar shear stress, the damage usually begins at the cord end point. In order to further improve the optimization effect, the D-P

hypothesis is used as the optimization criterion, and the von Mises of the cord end point is used as the evaluation index. The stress concentration of the cord end point at the bead is further optimized, and the von Mises of the main target cord end point is further optimized. At the same time, the interlaminar shear stress of the optimized cord end point is analyzed. The optimization results are shown in Figure 17.

First, the S12 shear stress was verified when equivalent stress was used as the optimization evaluation criterion and von Mises hypothesis was used as the optimization criterion in the initial

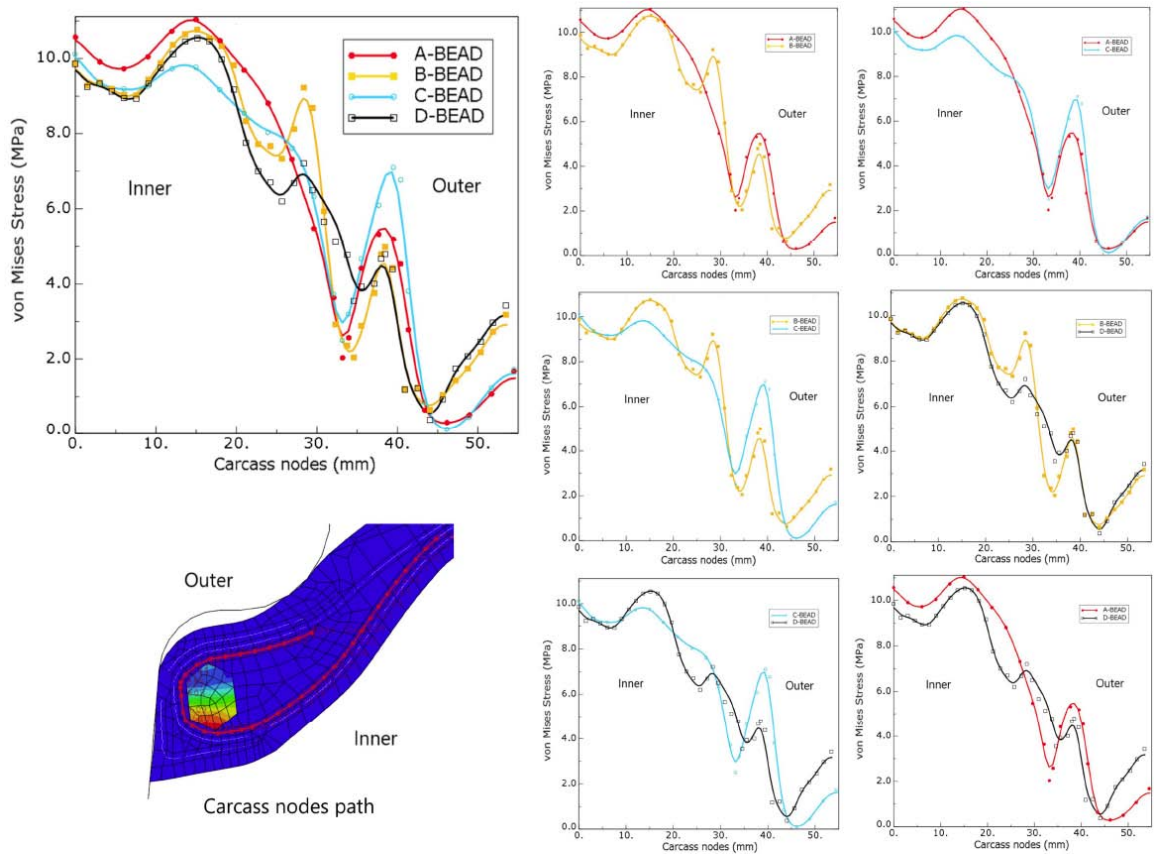


Figure 16: The von Mises stress analysis and comparison of the original quadrilateral bead A, hexagonal design bead B, optimized based on quadrilateral bead structure C, optimized based on hexagonal bead structure D on the carcass cord in the bead area.

Table 11: Optimization Results of Von Mises on the Inner and Outer Carcass Cords

Inner/mm	A-D/MPa	Pct	Outer/mm	A-D/MPa	Pct
3	0.5852	5.90%	34	-1.3600	-52.99%
6	0.7788	8.00%	36	0.4153	9.41%
9	0.7087	7.06%	38	0.6477	12.18%
12	0.6013	5.61%	40	0.3889	7.50%
15	0.4998	4.53%	42	0.1524	3.36%

optimization process. It can be intuitively seen from Fig. 4.27 that although the bead designed based on experience effectively reduces the shear stress value of the cord end of the outer bead, it increases the shear stress of the cord end of the inner bead. The subsequent optimization aims to reduce the shear stress of the cord end of the inner bead, and focuses on the shear stress of the cord end of the inner reinforcing layer of the bead. At the same time, it should be noted that the concave structure of the bead profile cannot be actually installed and used on the tire. The final optimization results are shown in Table 12 below:

On the basis of maintaining the von Mises stress at the end point of the carcass ply at the outer side of the bead area almost unchanged, the von Mises stress values at the end point of the cord at the inner and outer chafer of the bead area were optimized by 4.92% and 2.81%, respectively. On the basis of maintaining the S12 shear stress of the outer carcass ply and the end point of the chafer almost unchanged, the S12 shear stress value of the end point of the inner chafer of the bead area is optimized by 6.64%, which alleviates the stress increase caused by the end point of the inner chafer of the bead area in the previous optimization process. This optimization has made

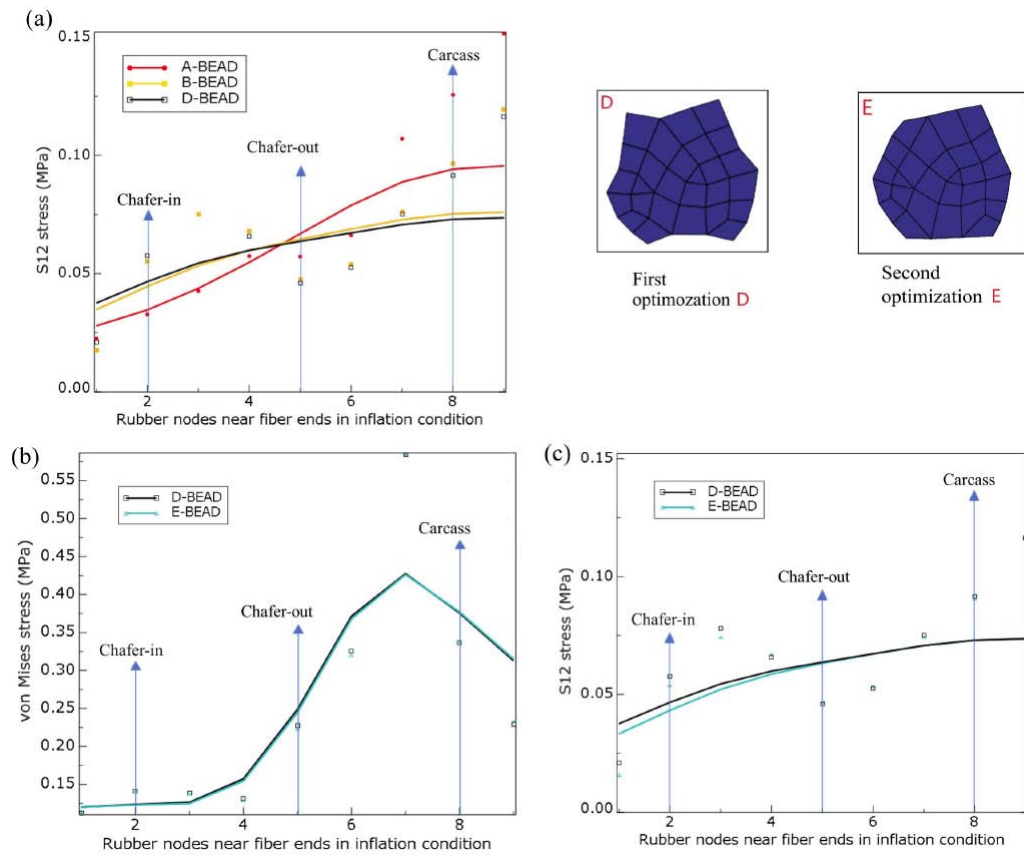


Figure 17: The effect analysis of secondary optimization: (a) the interlaminar shear stress S12 comparison after the first optimization of the cord endpoints in each structural bead area; (b) von Mises contrast after secondary optimization; (c) comparison of interlaminar shear stress S12 after secondary optimization.

Table 12: The Optimization Value and Optimization Effect of Von Mises and Interlaminar Shear Stress S12 at the End of the Cord in the Bead Area After the Secondary Optimization

von Mises	D-E(MPa)	PCT	S12	D-E(MPa)	PCT
Chafer-in	0.0070	4.92%	Chafer-in	0.0038	6.64%
Chafer-out	0.0064	2.81%	Chafer-out	-0.0007	-1.56%
Carcass	-0.0026	-0.76%	Carcass	0.0010	1.11%

constraints on the concave phenomenon of the bead profile, so that it meets the requirements of the production process, and effectively alleviates the increase of S12 shear stress at the end of the inner chafer of the bead area during the previous optimization process.

6.4. The Interlaminar Shear Stress of Cord Ends in the Bead Area Was Optimized For The Third Time

In order to obtain a better and more reasonable bead structure, the Tresca criterion is used as the optimization criterion in this optimization iteration process. The optimization objective is the S12 shear stress at the end of the bead area cord. Since S23 and

S13 are not the main interlaminar shear stresses of the tire, S23 and S13 are no longer redundantly analyzed and verified in this optimization design process. The optimization effect is shown in Figure 18.

As shown in Table 13, the final optimized structure F is compared with the secondary optimized structure E, and the von Mises and Tresca stresses at the ends of the bead area are optimized to be 4.17% and 4.45%, respectively. The S12 shear stress optimization of the inner and outer ends of the chafer is 12.65% and 9.86%, respectively, and other indicators are basically unchanged, and the ideal optimization results are obtained.

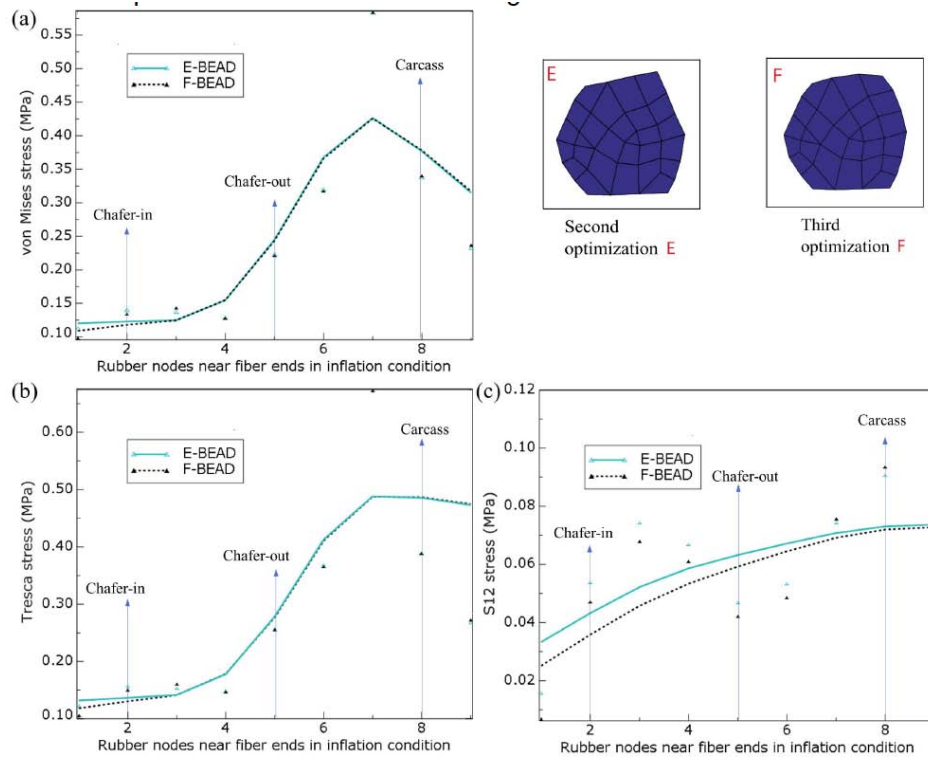


Figure 18: Analysis and comparison of (a) von Mises, (b) Tresca and (c) interlaminar shear stress S12 after third optimization.

Table 13: The Optimization Values and Effects of Von Mises, Tresca and Interlaminar Shear Stress S12 After Third optimization

E-F	von Mises (MPa)	PCT	Tresca (MPa)	PCT	S12 (MPa)	PCT
Chafer-in	0.0058	4.17%	0.0070	4.45%	0.0068	12.65%
Chafer-out	0.0022	0.99%	0.0026	1.00%	0.0046	9.86%
Carcass-out	-0.0013	-0.39%	-0.0015	-0.39%	-0.0029	-3.22%

On the basis of maintaining the optimization effect of reducing the von Mises stress concentration at the end point of the carcass cord at the outer side of the bead area during the previous optimization process, the optimized structure finally obtained further improves the interlaminar shear stress at the end point of the inner and outer chafer of the bead area. The main goal of this optimization design is to reduce the S12 interlaminar shear stress at the end point of the carcass cord in the bead area. The improvement of the S12 at the inner and outer ends of the chafer helps to further improve the ability of the bead area to resist shear damage. At the same time, it also proves that a variety of optimization evaluation criteria complement each other and can obtain a more ideal bead structure.

6.5. Optimization Design Has Effect Verification

In the optimization design of the bead, it is necessary to go through multiple rounds of optimization

design to get the final design scheme that meets the requirements. In the process of optimization design. Although the two-dimensional graphics can reflect the design of the solid model to a large extent, the solid model has the characteristics of three-dimensional space. The two-dimensional model cannot fully express all its information, and the two-dimensional model cannot simulate the contact process between the tire and the road surface. Therefore, in the optimization design, it is necessary to verify the design results obtained in the two-dimensional model in the three-dimensional solid model to ensure that its performance in the actual working conditions meets the requirements.

As shown in Figure 19, the two-dimensional axisymmetric cross-section model of the tire of structure F and the original structure A are finally compared and simulated. The optimized structure is reconstructed into a two-dimensional model to avoid

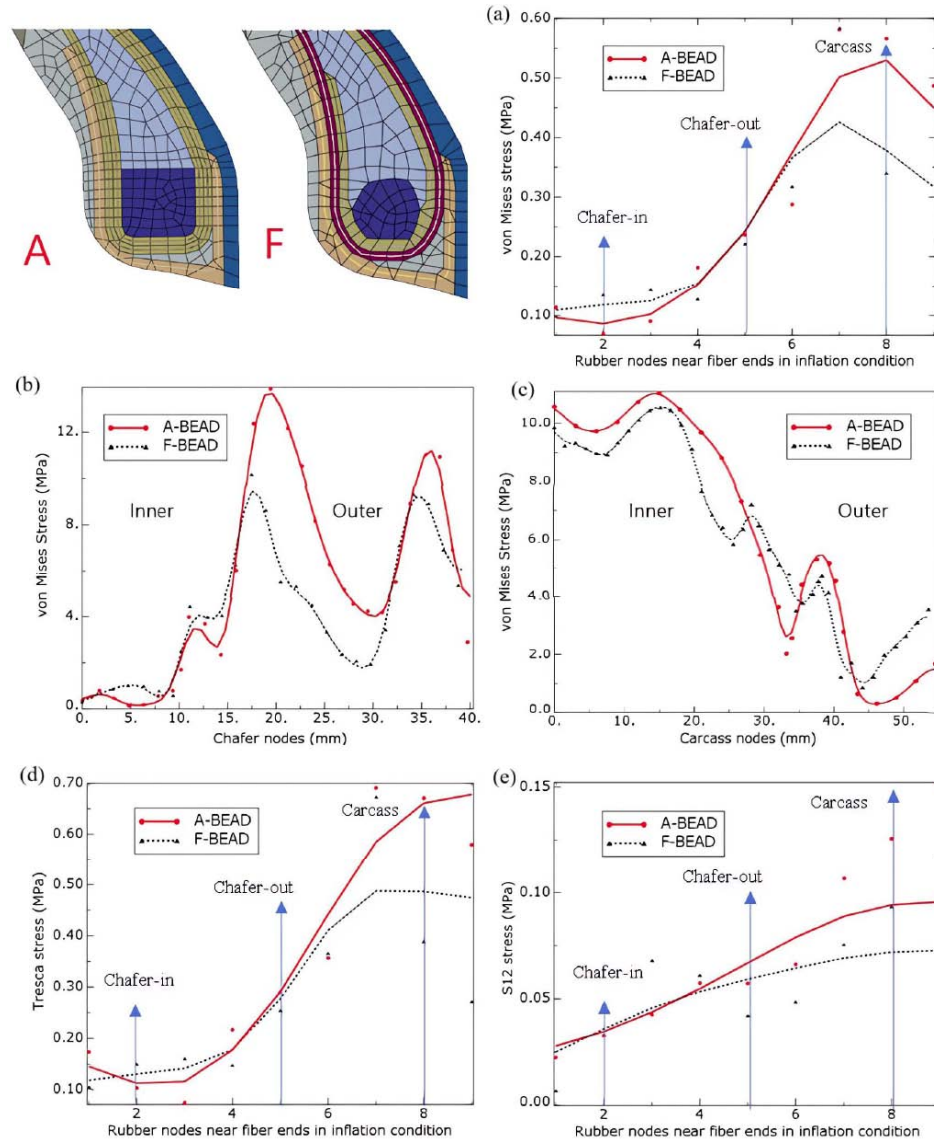


Figure 19: 265/25R18 tire whole bead optimization in 2D axisymmetric model simulation analysis: (a) von Mises stress of the rubber at the endpoints of the cord; (b) von Mises stress on the chafer cord; (c) von Mises stress on the carcass cord; (d) Tresca stress of the rubber at the endpoints of the cord; (e) S12 interlaminar shear stress of the rubber at the endpoints of the cord.

the analysis error caused by the mesh deformation of other structures at the tire bead area during the optimization process. Under the inflation condition of 0.29 MPa internal pressure, the results of analysis and verification in the two-dimensional axisymmetric 265/35R18 tire cross-section model are as follows: the von Mises at the cord end of the outer chafer of the bead area is reduced by 6.59%, Tresca is reduced by 12.27%, and S12 shear stress is reduced by 26.35%; the von Mises, Tresca and S12 shear stress at the end of carcass ply decreased by 39.98%, 42.01 %, and 25.62%, respectively. The von Mises, Tresca and S12 shear stress at the end of the inner chafer of the bead area increased by 0.0651 MPa (93.96%), 0.0468 MPa (45.51%) and 0.0143 MPa (43.53%), respectively. The

von Mises on the inner carcass cord decreased by 4.55% to 7.96%, and the von Mises on the outer carcass cord decreased by 2.27% -12.03%. The von Mises on the inner chafer cord decreased by 26.70%, and the von Mises on the outer chafer cord decreased by 15.66%.

As shown in Figure 20, because the two-dimensional model only simulates the inflation state of the tire, the optimization analysis results under the plane inflation cannot represent the same performance improvement of the optimized structure in the actual working process. Therefore, after the reconstruction of the three-dimensional model, after the inflation is completed, the radial load of 8590.6250 N is loaded

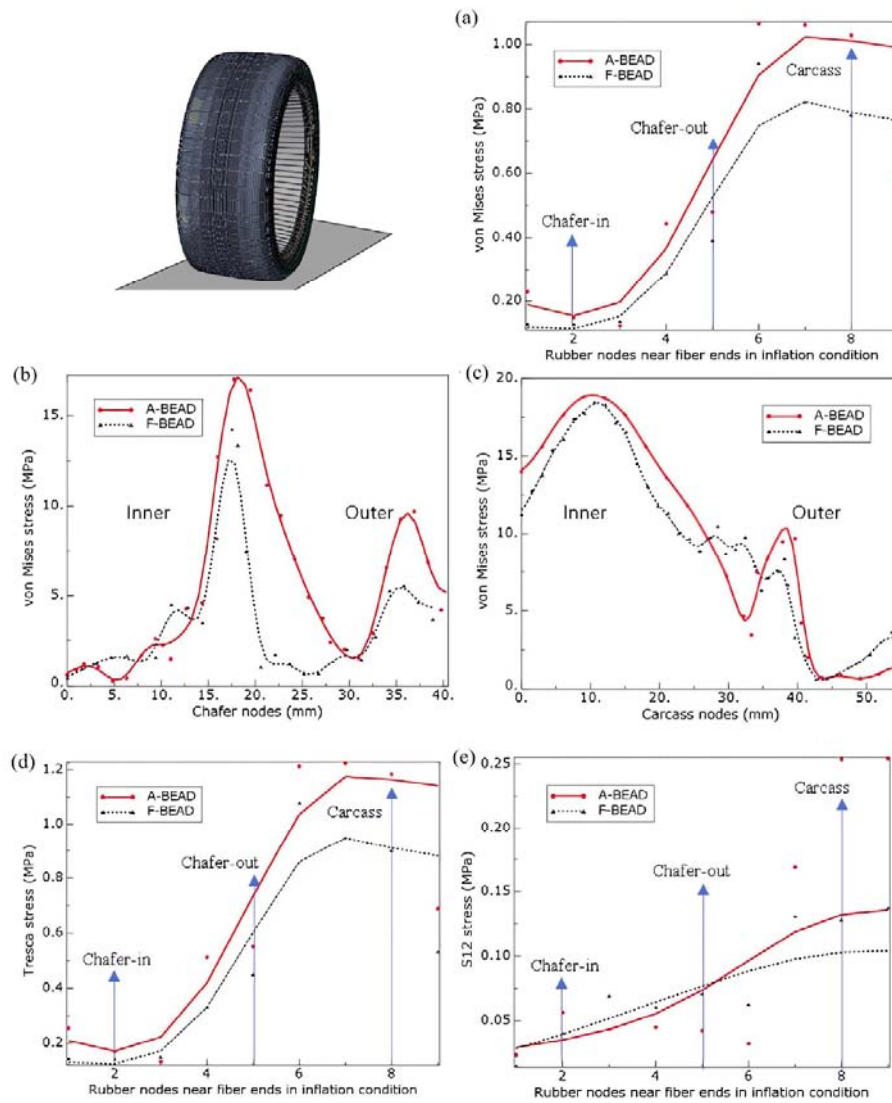


Figure 20: 265/25R18 tire whole bead optimization in 3D model simulation analysis: (a) von Mises stress of the rubber at the endpoints of the cord; (b) von Mises stress on the chafer cord; (c) von Mises stress on the carcass cord; (d) Tresca stress of the rubber at the endpoints of the cord; (e) S12 interlaminar shear stress of the rubber at the endpoints of the cord.

and the torsion is 15. Under the simulation conditions, the results of analysis and verification in the three-dimensional solid tire model are as follows: the von Mises of the cord end point of the outer chafer of the port is reduced by 18.52 %, and the Tresca is reduced by 18.56 %; the von Mises, Tresca and S12 shear stress at the end of the carcass ply layer on the outer side of the trochanter decreased by 24.12 %, 23.87 % and 49.51 %, respectively. The von Mises, Tresca and S12 shear stress at the end of the inner chafer cord of the bead area decreased by 14.48 %, 16.69 % and 28.96 %, respectively. The von Mises on the inner carcass cord decreased by 7.71 % to 14.66 %, and the von Mises on the outer carcass cord decreased by 15.48 % to 20.51 %. The von Mises on the inner chafer cord decreased by 13.17 %, and the von Mises on the outer chafer cord decreased by 40.36 %.

7. SUMMARY

The majority of radial tire disease occurs in the shoulder, sidewall, and bead areas, with the bead area accounting for approximately 30% of the damage. As the most significant load-bearing component of the bead area, the structural change of the bead is closely related to the bead's stress distribution. This paper analyzes the damage failure mechanism of the cord-reinforced composite structure in the tire from the common damage phenomenon of the cord end point in the tire bead area, establishes the composite material analysis model describing the end point of the carcass cord, and proposes an empirical design for a 265/35R18 truck and bus radial tire. The appropriate optimization criteria for the structural design of carcass cord-reinforced composites are investigated. The von

Mises criterion and the interlaminar shear stress criterion serve as the primary optimization criteria, with the D-P criterion added to increase the number of design iterations for optimization. Before and after vulcanization, the geometric mapping of tire structure was examined. The simulation model of a tire was developed, and its accuracy was validated by comparing the model to a stiffness experiment. The proposed experience-based overall bead structure performs well, but the experience-based design is insufficient. The proposed experience-based overall bead structure is designed to address the difficulty of obtaining a precise bead structure. The empirical design bead is topologically optimized on a two-dimensional axisymmetric cross-section model following a simulation-based analysis of the design's specific defects. For verification and analysis, the optimization results are reconstructed into a three-dimensional solid tire model. The ultimate effect of optimization is summarized as follows:

- (1) The von Mises of the inner and outer ends of the cord of the chafer decreased by 14.48% and 18.52%, respectively. The shear stress between the inner ends is reduced by 28.96%.
- (2) The von Mises on the inner and outer sides of the cord of the chafer decreased by 13.17% and 40.36%.
- (3) The von Mises of the end point of the carcass cord decreased by 24.12%, and the interlaminar shear stress decreased by 49.51%.
- (4) The von Mises on the inner and outer sides of the carcass cord decreased by 7.71% to 14.66% and 15.48% to 20.51%, respectively.

The optimization design effectively alleviates the stress concentration on the cord in the tire bead region, improves the fracture resistance of the cord, reduces the von Mises and interlaminar shear stress levels at the end of the vulnerable cord, and prevents the damage cracks of the cord-reinforced composite material caused by the interlaminar deformation coordination effect. The optimized overall bead structure can smooth the stress distribution on the carcass cord, reduce the stress concentration of the carcass cord, make the stress distribution of the material around the cord end more reasonable, and provide a more uniform stress distribution, thereby decreasing the chance of steel cord damage. This optimization can enhance the tire's bearing capacity

under working conditions, the tire's strength and durability, the tire's resistance to early damage, and the tire's performance and safety performance during use.

ACKNOWLEDGEMENTS

This work was supported by Qingdao Natural Science Foundation (Grant No. 23-2-1-218-zyyd-jch).

REFERENCES

- [1] Zhang S, Han S, Zhang K, Chen L, Li Y. Study on optimizing transition layer thickness to reduce tire sidewall delamination. *Journal of Physics: Conference Series*. IOP Publishing 2023; 012040. <https://doi.org/10.1088/1742-6596/2483/1/012040>
- [2] Li Y, Sun X, Zhang S, Miao Y, Han S. Experimental investigation and constitutive modeling of the uncured rubber compound based on the DMA strain scanning method. *Polymers* 2020; 12: 1-12. <https://doi.org/10.3390/polym12112700>
- [3] Zhang Y, Wang Y, Jiang Z, Zheng L, Chen J, Lu J. Subdomain adaptation network with category isolation strategy for tire defect detection. *Measurement* 2022; 204: 112046. <https://doi.org/10.1016/j.measurement.2022.112046>
- [4] Linden M, Eckstein L, Schlupek M, Duning R. Investigation of the pressure distribution between tire bead and rim flange under static load conditions-untersuchung der druckverteilung zwischen reifenwulst und felgenhorn unter statischen lastzustanden. *VDI Berichte* 2022; 2022: 97-116. <https://doi.org/10.51202/9783181023983-97>
- [5] Zhang N, Lin JY, Liu XY, Xing LJ, Hao YH. Finite element analysis on bead crack in radial tire. *Journal of Highway and Transportation Research and Development* 2019; 36: 144-150. <https://doi.org/10.3969/j.issn.1002-0268.2019.04.020>
- [6] Baranowski P, Malachowski J, Mazurkiewicz Ł. Local blast wave interaction with tire structure. *Defence Technology* 2020; 16: 520-529. <https://doi.org/10.1016/j.dt.2019.07.021>
- [7] Yu B, Xing C, Cai Y. Structural optimization design for improving aging durability of light truck and bus radial tire. *Tire Industry* 2020; 40: 588-592. <https://doi.org/10.12135/j.issn.1006-8171.2020.10.0588>
- [8] Palika P, Huady R, Hagara M, Lengvarsky P. Optimization of apex shape for mounting to the bead Bundle using FEM. *Materials* 2023; 16: 377-377. <https://doi.org/10.3390/ma16010377>
- [9] Jiang H, Sun Z, Liu C. Finite element study on factors affecting bead durability of all-steel radial tire. *Tire Industry* 2019; 39: 525-531. <https://doi.org/CNKI:SUN:LTGY.0.2019-09-002>
- [10] Sanjeev kumar R, Vetrivel kumar K, Ramakrishnan T. Design optimization of airless tyre - Numerical Approach. *IOP Conference Series: Materials Science and Engineering* 2021; 1057: 12-32. <https://doi.org/10.1088/1757-899X/1057/1/012032>
- [11] Li Y, Sun X, Song J, Zhang S, Han S. Topological structure and experimental investigation of a novel whole tire bead. *Materials & Design* 2021; 203: 109592. <https://doi.org/10.1016/j.matdes.2021.109592>
- [12] Li Y, Zhang S, Feng Q, Qi S, Han S, Chen L. Topological shape optimisation of a novel whole bead structure based on an interlaminar shear stress criterion. *International Journal of Mechanics and Materials in Design* 2022; 18: 961-974. <http://dx.doi.org/10.1007/s10999-022-09614-9>

- [13] Haichao H, Qiang W, Boya L, et al. Progressive damage behaviour analysis and comparison with 2D/3D hashin failure models on carbon fibre-reinforced aluminium laminates. *Polymers* 2022; 14: 29-46. <https://doi.org/10.3390/POLYM14142946>
- [14] Cardim HP, Minillo LQ, Nakao F, Ortenzi A. Dynamic elastic modulus variability in anisotropic and isotropic materials: comparison by acoustic emission. *Journal of Research Updates in Polymer Science* 2023; 12: 19-26. <https://doi.org/10.6000/1929-5995.2023.12.01>
- [15] Pino GGD, Bezazi A, Boumediri H, et al. Numerical and experimental analyses of hybrid composites made from amazonian natural fiber. *Journal of Research Updates in Polymer Science* 2023; 12: 10-18. <https://doi.org/10.6000/1929-5995.2023.12.02>
- [16] Yungao R, Zeng M, Huanlin Z. Structural optimization design of non-uniform stiffened cylindrical shells with geometric imperfection. *Journal of Applied Mechanics* 2021; 38: 458-464. <https://doi.org/10.11776/cjam.38.02.C028>
- [17] Jianping Y, Liwei Z, Zhijun W, Yongjia X, You M. Optimizing design of a multi-mode warhead. *Ordnance Material Science and Engineering* 2014; 37: 15-18. <https://doi.org/10.14024/j.cnki.1004-244x.2014.01.034>
- [18] Pagani A, Azzara R, Wu B, Carrera E. Effect of different geometrically nonlinear strain measures on the static nonlinear response of isotropic and composite shells with constant curvature. *International Journal of Mechanical Sciences* 2021; 209: 106713. <https://doi.org/10.1016/j.ijmecsci.2021.106713>
- [19] Li Q, Li H. Continuum structure topology optimization method based on improved SIMP method. *Journal of Mechanical & Electrical Engineering* 2021; 38: 428-433. <https://doi.org/10.3969/j.issn.1001-4551.2021.04.004>
- [20] Dong L, Wu X. Integrated topology optimization of materials and structures based on variable density method. *Journal of Mechanical & Electrical Engineering* 2020; 37: 1109-1114. <https://doi.org/CNKI:SUN:JDGC.0.2020-09-021>
- [21] Huang Y, Li C, Meng X, Yong Z. FEA optimization design of belt cord for 235/45R18 tire. *China Rubber Industry* 2020; 67: 209-213.
- [22] Feng Q, Yong Z. Finite element optimization design of 12R22.5 tire belt cords. *China Elastomerics* 2021; 31: 29-33. <https://doi.org/10.16665/j.cnki.issn1005-3174.2021.04.006>
- [23] Heyman. *Elements of stress analysis*. Cambridge: Cambridge University Press, 1982.
- [24] Xue G. Analysis of mechanical properties of welded joints based on mises yield criterion and I₁ fracture criterion. *Development and Application of Materials* 2022; 37: 1-10. <https://doi.org/10.19515/j.cnki.1003-1545.2022.05.015>
- [25] Maciej B, Jan G, Aleksandra B, Krzysztof W. Numerical simulation of dry ice compaction process: comparison of Drucker-Prager/Cap and cam clay models with experimental results. *Materials* 2022; 15: 5771-5771. <https://doi.org/10.3390/MA15165771>
- [26] Guo J, Yang Q, Lu X, et al. Research on generalized unified strength theory of rock (mass) failure. *Journal of China Coal Society* 2021; 46: 3869-3882. <https://doi.org/10.13225/j.cnki.jccs.2021.0245>
- [27] Tsao CC, Hocheng H. A review of backup mechanism for reducing delamination when drilling composite laminates. *Journal of Research Updates in Polymer Science* 2016; 5: 97-107. <https://doi.org/10.6000/1929-5995.2016.05.03.2>
- [28] Schoeffer J. An accurate and refined beam model fulfilling the shear and the normal stress traction condition. *International Journal of Solids and Structures* 2022; 243. <https://doi.org/10.1016/j.ijsolstr.2022.111535>
- [29] Zhuang H, Wang J, Gao Z. Anisotropic and noncoaxial behavior of soft marine clay under stress path considering the variation of principal stress direction. *International Journal of Geomechanics* 2022; 22: 04022062. [https://doi.org/10.1061/\(ASCE\)GM.1943-5622.0002390](https://doi.org/10.1061/(ASCE)GM.1943-5622.0002390)
- [30] Peng C Y, Zeng J C, Xiao J Y, Gang D U. Analytic solutions to mean interlaminar shear stress of cross-ply laminate under compression loads. *Fiber Reinforced Plastics/Composites* 2006: 3-6.
- [31] Zhang Q, Shi J, Suo S, Meng G. Finite element analysis of rubber materials based on Mooney Rivlin model and Yeoh model. *China Synthetic Rubber Industry* 2020; 43: 468-471.
- [32] Chen JS, Wu CT, Pan C. A pressure projection method for nearly incompressible rubber hyperelasticity, Part II: applications. *Journal of Applied Mechanics* 1996; 63: 869-876. <https://doi.org/10.1115/1.2787241>

Received on 10-06-2023

Accepted on 14-07-2023

Published on 19-07-2023

<https://doi.org/10.6000/1929-5995.2023.12.06>

© 2023 Li et al.; Licensee Lifescience Global.

This is an open access article licensed under the terms of the Creative Commons Attribution License (<http://creativecommons.org/licenses/by/4.0/>) which permits unrestricted use, distribution and reproduction in any medium, provided the work is properly cited.